Computational Analysis of a Quiet Single-Main Rotor Helicopter for Air Taxi Operations

Patricia Ventura Diaz
Science and Technology Corporation
NASA Ames Research Center
Moffett Field, California, USA

David Garcia Perez
Science and Technology Corporation
NASA Ames Research Center
Moffett Field, California, USA

Seokkwan Yoon
NASA Advanced Supercomputing Division
NASA Ames Research Center
Moffett Field, California, USA

ABSTRACT

A computational study has been done on NASA's quiet single-main rotor helicopter concept for urban air mobility using high-fidelity computational fluid dynamics, rotorcraft comprehensive analysis tools, and computational aeroacoustics. High-order accurate schemes, dual-time stepping, and the delayed detached-eddy simulation model have been employed. A loose-coupling approach between the flow solver and the rotorcraft comprehensive code is implemented to include vehicle trim and blade motions. Acoustic simulations based on the Ffowcs-Williams and Hawkings equations have been performed to compute the rotor noise. Different blade geometries and tip speeds are analyzed, and performance and acoustics results are compared. The vehicle has been simulated in hover and cruise, with flight conditions representative of an air taxi mission. The quiet single-main rotor helicopter is one of the conceptual designs intended to focus and guide NASA's research activities in support of aircraft development for vertical take-off and landing air taxi operations.

NOMENCLATURE

Acronyms

Acronym	Description
BVI	Blade-vortex interaction
EPNL	Effective perceived noise level
FM	Figure of merit
NB	Near-body
OB	Off-body
QSMR	Quiet single-main rotor
SPL	Sound pressure level
UAM	Urban air mobility
WMTO	Maximum take-off weight

Greek symbols

Symbol	Description
β_0	Coning angle
β_{1c}	Longitudinal flapping angle
β_{1s}	Lateral flapping angle
Δ	Grid spacing
δ	Boundary layer thickness
μ	Advance ratio
Ω	Rotor rotational speed
ψ	Azimuth position
ρ	Fluid density
σ	Thrust-weighted solidity
θ_0	Collective angle
θ_{tw}	Linear twist

Roman symbols

Symbol	Description
a	Fluid speed of sound
c	Local rotor blade chord length
C'	Sectional blade chord force
d	Turbulent length scale
h	Flight altitude
L/D_e	Effective lift-to-drag ratio
M	Mach number
M'	Sectional blade pitching moment
M^2c_c	Sectional chord force coefficient
M^2c_m	Sectional pitching moment coefficient
M^2c_n	Sectional normal coefficient
N'	Sectional blade normal force
P	Rotor power
p_0	Reference pressure
p_{rms}	Frequency-weighted pressure
R	Rotor radius
r	Radial position
Re	Reynolds number
T_∞	Freestream temperature
V	Velocity
y^+	Non-dimensional viscous wall spacing

Subscripts

Subscripts	Description
∞	Freestream
root	Blade root
tip	Blade tip

INTRODUCTION

Urban Air Mobility (UAM) air taxi vehicles have grown very popular over the past few years. Conventional and more unconventional concept vehicles are being developed by the industry, including configurations such as tiltwing, quadcopters, ducted rotors, tilt-rotors, ducted-fans, distributed propulsion, etc. UAM envisions a new aviation transportation system with highly automated and safe vehicles that will transport passengers and cargo in the urban and suburban areas. In addition, by using hybrid or electric propulsion, UAM vehicles will provide a greener means of transportation.

NASA's Revolutionary Vertical Lift Technology (RVLT) project has been developing tools and datasets to support the design of advanced vertical-lift aircraft (Ref. 1). RVLT is designing several UAM concept vehicles, with the objective to focus and guide the research activities in support of aircraft development for emerging aviation markets (Refs. 2–4). RVLT has also been elaborating various software packages to link individual discipline-based prediction tools into a unified toolchain. RVLT toolchain has been applied to several concept vehicles for the practical design of quieter UAM aircraft (Ref. 5). The concept vehicles include quadrotor, side-by-side, lift+cruise, and tiltwing configurations. While most of the vehicle designs considered for UAM have multiple rotors, an often disregarded configuration is the single-main rotor helicopter, despite its importance for its known path for certification. In this paper, the quiet single-main rotor (QSMR) helicopter concept based on the work by Johnson (Ref. 6) will be analyzed by using high-fidelity Computational Fluid Dynamics (CFD) and computational aeroacoustics (CAA). The QSMR vehicle, shown in Figure 1, consists of a single-main rotor helicopter with a NOTAR (NO TAil Rotor) anti-torque system, instead of a tail rotor to remove tail-rotor noise. It has specifically been designed for low-noise operations.

Figure 1: Quiet single-main rotor helicopter.

The accurate prediction of rotorcraft performance and acoustics is very challenging from a computational point of view: the flows are unsteady, nonlinear, and complex. In the case of multi-rotor vehicles, the aerodynamic interactions between the rotors (and other components when simulating the complete vehicle) make the problem even more difficult. While low-fidelity tools offer the advantage of a short turn-around and low computational cost, only with high-fidelity methods the complex flow details and the aerodynamic interactions can be captured. In addition, high-fidelity simulations can provide the information needed to calibrate the lower fidelity tools that can be used for design purposes.

Previous high-fidelity CFD work performed by Ventura Diaz *et al.* (Refs. 7–10) includes simulations of NASA's quadrotor isolated rotors (Ref. 7) and quadrotor complete vehicle (Ref. 8), NASA's side-by-side air taxi concept (Ref. 9), and computational analysis of small multi-rotor vehicles (Ref. 10). Li *et. al* performed an acoustics analysis of the QSMR using lifting-line loading distribution and a dual-compact thickness noise model (Ref. 11).

The QSMR vehicle is designed to carry a payload of 1200 lb or up to six passengers (including the pilot if not autonomous). The mission consists of two 37.5 nm flights with a 20 min reserve (Ref. 6). Three configurations are simulated —baseline, low-noise without blade droop, and low-noise with 30° droop— that mainly differ in the blade geometry and design tip speed. The parameters that define each configuration are extracted from Johnson's acoustic analysis of the QSMR (Ref. 6). From its findings: "designing the aircraft with a tip speed of 450 ft/s reduced the approach effective perceived noise level (EPNL) by 12 dB relative a design for 700 ft/s, with only a small increase in aircraft weight". Also, it was found that 30° droop of the blade tip further reduced the approach noise. With a lower tip speed for the low-noise configuration, the number of blades is increased from three to six to maintain the blade aspect ratio (with higher solidity).

The objectives of the present work are to simulate and analyze NASA's QSMR UAM concept using high-fidelity CFD and CAA. First, the QSMR is studied using free wake model in a rotorcraft comprehensive code. Acoustics simulations based on the Fwocs-Willians and Hawkings equation are carried out with the information from the free wake solution. Then, the QSMR high-fidelity CFD simulations are performed, and the flow solver is coupled with the comprehensive rotorcraft code for accurate prediction of blade motions and airloads. Design parameters like the rotor tip speed and blade geometry are studied, and the rotor wake geometry, airloads, performance, and acoustics are analyzed for each case.

NUMERICAL APPROACH

The flow solver used in this study is NASA's OVERFLOW (Ref. 12) CFD solver. OVERFLOW is a finite-difference, structured overset grid, high-order accurate Navier-Stokes flow solver. NASA's Chimera Grid Tools (CGT) (Ref. 13) overset grid generation software is used for generating the overset grids of rotors and complete vehicles. Body-fitted curvilinear near-body (NB) grids are generated using CGT. The computational domain is completed with the generation of Cartesian off-body (OB) grids that are automatically generated prior to grid assembly using the domain connectivity framework in OVERFLOW-D mode. The current time-accurate approach consists of an inertial coordinate system where NB curvilinear O-grids for the rotor blades rotate through the fixed OB Cartesian grid system. OVERFLOW is loosely coupled with the helicopter comprehensive code CAMRAD II (Ref. 14). The CFD provides high-fidelity, nonlinear aerodynamics that corrects the comprehensive lifting line aerodynamic analysis from CAMRAD II. The comprehensive code performs the

structural dynamics and trim calculations and gives the information to OVERFLOW. The loose coupling allows for a modular approach and communication through input/output. NASA's second-generation Aircraft Noise Prediction Program (ANOPP2) (Ref. 15) is used to calculate the acoustics. The thickness, loading, broadband, propagation, and observer noise can be calculated with ANOPP2.

The numerical approach and the coupling process are described in more detail in the following paragraphs.

Overset Grid Generation

The overset grid generation process using CGT may be decomposed into four steps: geometry processing, surface grid generation, volume grid generation, and domain connectivity (Ref. 13).

The geometry is usually obtained from a computer-aided design (CAD) model or a 3D-scanning point cloud. In solid modeling, the boundary representation (BRep) of an object describes its boundaries holding both the topological entities and the geometric components (Ref. 16). A pre-processing step generates discrete surface representations from the analytical BRep solid contained in STEP or IGES files. Access to the model topology and entities is accomplished through EGADS (the Engineering Geometry Aircraft Design System) API, which is a foundational component of the Engineering Sketch Pad (Ref. 16). For each body in the geometry, the `egads2srf` tool generates a surface grid file containing a set of structured surface patches on tessellated untrimmed BRep faces. The CAD model for the QSMR fuselage is shown in Figure 2a. Figure 2b shows the structured untrimmed patches obtained using EGADS. A curve grid file is also created that contains structured curves on tessellated BRep edges. Both files are used as inputs in the overset surface grid generation step.

Once the geometry has been processed as reference curve and surface files, structured surface grids are generated using a combination of algebraic and hyperbolic methods. The generation of surface grids is the step that requires the most manual effort and experience from the user. Figure 3 shows the overset surface grids for the three configurations of the quiet single-main rotor UAM concept studied in this work: "baseline" (Figure 3a), "low-noise no blade droop" (Figure 3b), and "low-noise 30° blade droop" (Figure 3c). The complete vehicle consists of the rotor, hub, landing gear, tail, and fuselage. The physics of the NOTAR are not modeled in the CFD simulations, but they are included in the comprehensive analysis for correct vehicle trim.

If surface grids have sufficient overlap, the volume grids are then created using hyperbolic marching methods which extend the grid out to a fixed distance from the surface. Tight clustering in the normal direction near the wall is maintained to achieve good boundary layer resolution in viscous flow computations. The normal grid spacing of all grids at the walls maintains $y^+ \leq 1$. Mesh orthogonality is maximized to provide better solution accuracy. NB volume grids are extended ensuring that the outer boundaries are outside the boundary layer. The NB grids are contained inside the OB Cartesian grids, which extend to the far-field.

Uniform spaced off-body Cartesian grids are utilized to resolve important flow features such as the wake region. Many Cartesian grids with successive levels of refinement based on proximity to the body are generated. Each Cartesian grid is twice as coarse as the previous level, and they expand the grid system to the far-field. The uniform spacing of the first OB grid layer, which contains the resolved wake region, is 12.0 % of the blade tip chord length c_{tip}. Cartesian grids extend to the far-field boundary, which is 20 radii away from the center of the vehicle in all directions.

While airframe grids are generated from the CAD model shown in Figure 2a, blade grids are generated from the information in Table 1. It summarizes the rotor blade geometry properties for the baseline case ($V_{\text{tip}} = 700\,\text{ft/s}$) and the low-noise case ($V_{\text{tip}} = 450\,\text{ft/s}$) with and without tip droop. The blades use a modern, 11 % thick airfoil, with $\theta_{\text{tw}} = -12°$ twist and 60 % tapered tip (from $0.94R$). The root cutout is $0.15R$. The transition between the two different airfoil sections is smooth —linear interpolation with the radial stations—. The blades from the low-noise configuration with droop have a droop tip of 30° applied at $r = 0.94R$.

Table 1: Quiet single main rotor geometry properties and design tip speed.

Parameter	**Baseline**	**Low-noise**
Number of blades/rotor	3	6
Radius R	5.170 m	5.378 m
Linear twist θ_{tw}	−12.0°	−12.0°
Root chord c_{root}	0.230 m	0.290 m
Tip chord c_{tip}	0.138 m	0.174 m
Thrust-weighted solidity σ	0.041	0.099
Design tip speed V_{tip}	700 ft/s	450 ft/s
WMTO	1663 kg	1841 kg

The blade grids for the three cases are shown in detail in Figure 4. Surface grid resolution on the rotor blades is clustered in the chordwise direction near the airfoils leading and trailing edges, regions characterized by large pressure gradients. By the same token, the spanwise direction is clustered near the blades' root and tip.

Domain connectivity issues occur in the overset grid approach as grids arbitrarily overlap with each other, and some points of a grid might lie in the interior of a neighboring component. The domain connectivity step is robust and highly automated when using a trimmed approach. The X-ray hole cutting approach is used in this work. An X-ray object is created for every component of the geometry, i.e., blades, fuselage, landing gear, etc. The user has to supply the list of meshes that each X-ray object is allowed to cut, and an offset distance with which to grow each hole away from the body. Hole cutting is required between components and with the off-body Cartesian grids. This process is performed at each time step within the flow

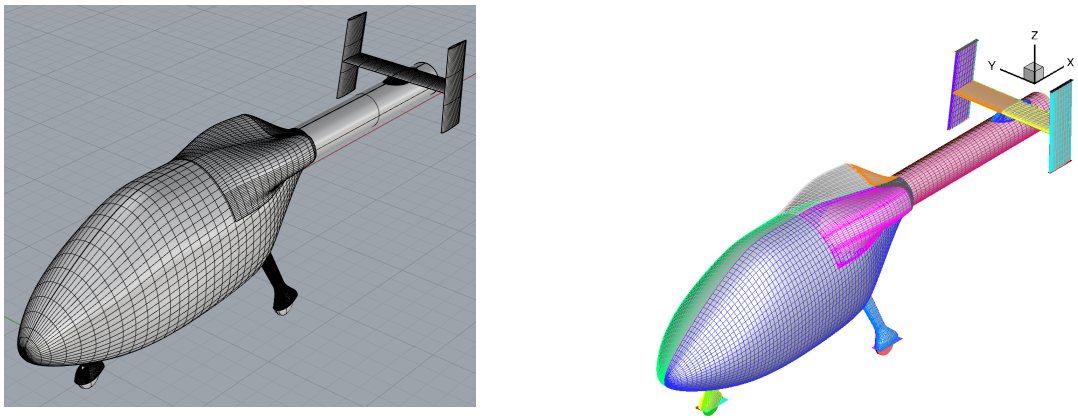

(a) CAD geometry.

(b) EGADS surface grid.

Figure 2: The quiet single main rotor fuselage. Figure 2a shows the CAD geometry. Figure 2b shows the structured untrimmed patches obtained from the CAD geometry using EGADS. The patches are used as reference surfaces to generate the overset surface grids.

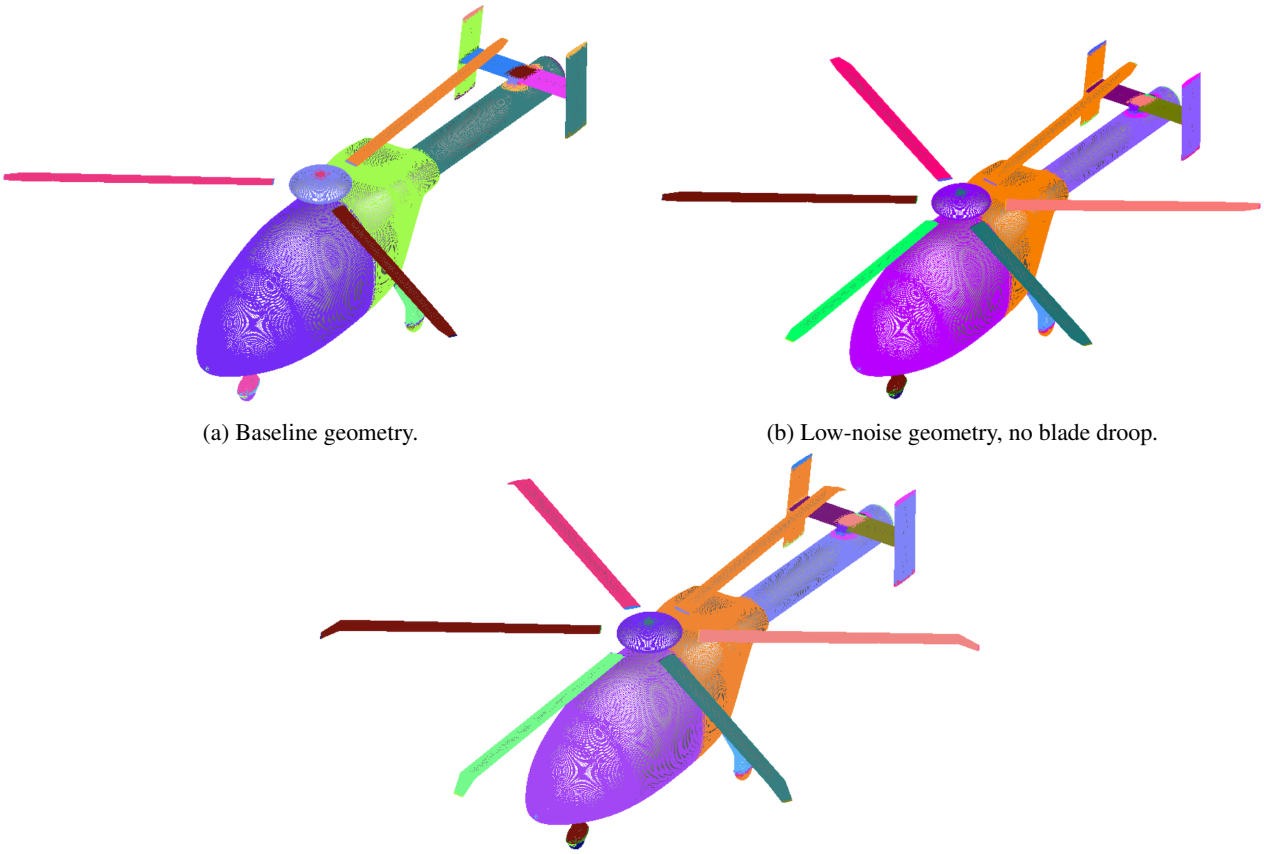

(a) Baseline geometry.

(b) Low-noise geometry, no blade droop.

(c) Low-noise geometry, 30° blade droop.

Figure 3: QSMR overset surface grids for the complete vehicle, which includes the main rotor, main rotor hub, fuselage, tail, and landing gear. Figure 3a shows the vehicle with the baseline rotor geometry, with three blades and $R = 5.170\,\text{m}$. Figure 3b shows the low-noise QSMR vehicle, with a six-bladed rotor, no droop, and $R = 5.378\,\text{m}$. A 30° blade droop is included for the QSMR vehicle in Figure 3c.

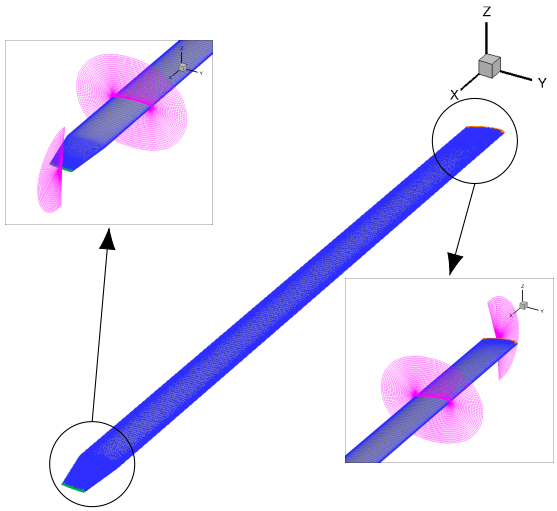

(a) Baseline geometry blade.

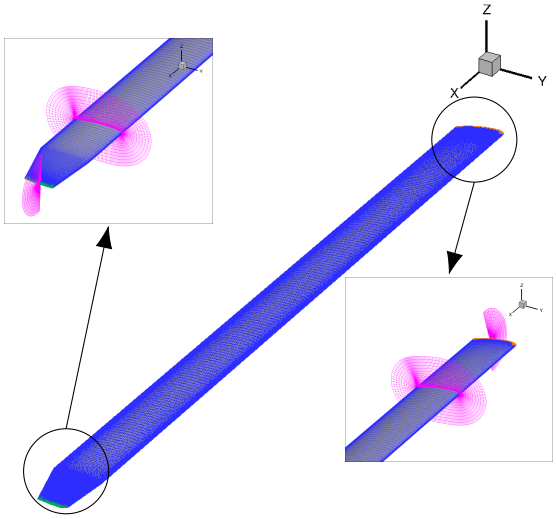

(b) Low-noise geometry blade, no blade droop.

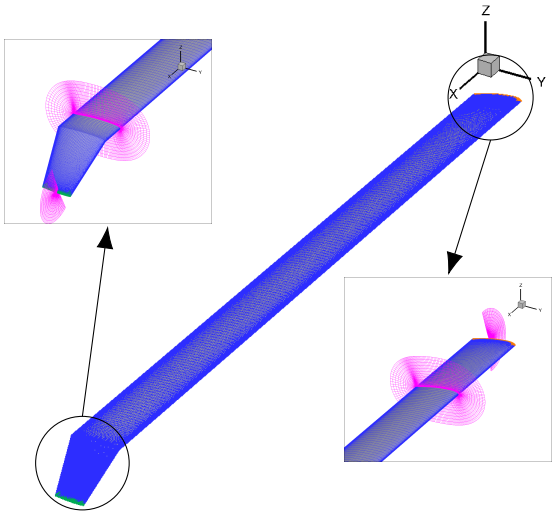

(c) Low-noise geometry blade, 30° blade droop at $r = 0.94R$.

Figure 4: Blade overset grids for the quiet single-main rotor helicopter. O-grids are used for the main blade grid. For the tip and root, cap grids are used. Grid clustering near the leading edge, trailing edge, blade tip and blade root is applied to solve the large pressure gradients near these regions. Figure 4a shows the baseline case. Figure 4b shows the low-noise no blade droop case. Figure 4c shows the low-noise 30° blade droop case.

Table 2: NB and OB grid features of all configurations studied.

Configuration	**NB grids**	**NB grid points**	**NB+OB grid points (hover)**
Baseline	64	94×10^6	678×10^6
Low-noise no droop	73	110×10^6	563×10^6
Low-noise 30° droop	73	112×10^6	564×10^6

solver, allowing the rotating components to move relative to the fixed components.

Table 2 shows the number of NB grids, and the number of points of NB and OB grids of each configuration analyzed.

High-Order Accurate Navier-Stokes Solver

The Navier-Stokes equations can be solved using finite differences with a variety of numerical algorithms and turbulence models. The time-dependent Reynolds-Averaged Navier-Stokes (RANS) equations are solved in strong conservation form:

$$\frac{\partial \vec{q}}{\partial t} + \frac{\partial(\vec{F}-\vec{F}_{\mathrm{v}})}{\partial x} + \frac{\partial(\vec{G}-\vec{G}_{\mathrm{v}})}{\partial y} + \frac{\partial(\vec{H}-\vec{H}_{\mathrm{v}})}{\partial z} = 0, \qquad (1)$$

being $\vec{q} = [\rho, \rho u, \rho v, \rho w, e]^{\intercal}$ the vector of conserved variables; $\vec{F}$, $\vec{G}$ and $\vec{H}$ the inviscid flux vectors; and $\vec{F}_{\mathrm{v}}$, $\vec{G}_{\mathrm{v}}$ and $\vec{H}_{\mathrm{v}}$ the viscous flux vectors.

In this study, the diagonal central difference algorithm is used with the 5$^{\mathrm{th}}$-order accurate spatial differencing option with scalar dissipation. The physical time step corresponds to 0.25° rotor rotation, together with up to 50 dual-time sub-iterations for 2.5 to 3.0 orders of magnitude drop in sub-iteration residual. The numerical approach and time step were previously validated for various rotor flows (Refs. 17–19).

Hybrid turbulence model

The OVERFLOW code currently includes algebraic, one-equation, and two-equation turbulence models, including the choice of hybrid Reynolds-Averaged Navier-Stokes / Large Eddy Simulation (RANS/LES) models that close the RANS equations. In this study, the one equation Spalart-Allmaras (Ref. 20) turbulence model is used primarily within the boundary layer.

The Detached Eddy Simulation (DES) (Ref. 20) approach provides a good compromise between realism and computational cost. The intent of this model is to combine efficiently the best aspects of RANS and LES methodologies in a single solution. Near-wall regions are treated in RANS mode since turbulent scales can be very small and need to be modeled; and the rest of the flow is treated in LES mode, where the largest turbulent scales are grid-resolved. In this way, DES is a RANS/LES hybrid approach that mitigates the problem of artificially large eddy viscosity. The turbulence length scale d is replaced by $\bar{d}$:

$$\bar{d} = \min(d, C_{\mathrm{DES}}\Delta), \qquad (2)$$

which is the minimum of the distance from the wall d and C_{DES} times the local grid spacing Δ.

The DES approach assumes that the wall-parallel grid spacing $\Delta_{||}$ exceeds the thickness of the boundary layer δ so that the RANS model remains active near solid surfaces. If the wall-parallel grid spacing is smaller than the boundary layer thickness, $\Delta_{||} < \delta$ then the DES Reynolds stresses can become under-resolved within the boundary layer; this may lead to non-physical results, including grid-induced separation. Using Delayed Detached Eddy Simulation (DDES) (Ref. 21), the RANS mode is prolonged and is fully active within the boundary layer. The wall-parallel grid spacing used in this study does not violate the hybrid-LES validity condition; thus, DES and DDES should give similar results. Nevertheless, all computations have been performed using the DDES model for both NB and OB grids.

Comprehensive Analysis

Structural dynamics and rotor trim for the coupled calculations are performed using the comprehensive rotorcraft analysis code CAMRAD II (Ref. 14). CAMRAD II is an aeromechanics analysis of rotorcraft that incorporates a combination of advanced technologies, including multibody dynamics, nonlinear finite elements, and rotorcraft aerodynamics. The trim task finds the equilibrium solution for a steady-state operating condition, and produces the solution for performance, loads, and vibration. The aerodynamic model for the rotor blade is based on lifting-line theory, using two-dimensional airfoil characteristics and a vortex wake model. CAMRAD II has undergone extensive correlation with performance and loads measurements on rotorcraft.

Loose Coupling OVERFLOW – CAMRAD II

A loose coupling approach between OVERFLOW and CAMRAD II based on a trimmed periodic rotor solution is implemented. The comprehensive code provides the trim solution and blade motions. The high-fidelity CFD calculates the airloads. That is, the CFD airloads replace the comprehensive airloads while using lifting line aerodynamics to trim and computational structural dynamics to account for blade deformations. Figure 5 summarizes the loose coupling approach.

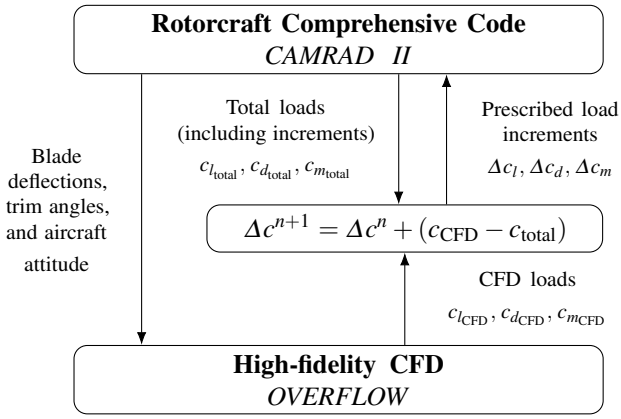

Figure 5: Flow diagram for CFD/Comprehensive Analysis loose coupling methodology.

The simulation is initialized with a comprehensive analysis resulting in a trimmed rotor solution obtained with lifting line aerodynamics. This analysis creates initial quarter chord motions as a function of the radial position r and the azimuth ψ, for the rotor. In addition, the aircraft attitude is also obtained

from CAMRAD II. The motions and aircraft pitch angle are given to the CFD. The CFD analysis accounts for the entire flow field, and therefore it only requires the structural motion. The CFD is run with the prescribed motions and angles, for two to three full rotor revolutions for the first coupling step. OVERFLOW outputs the normal force N' , pitching moment M' , and chord force C' as a function of radius and azimuth. Then, the aerodynamic force and moment coefficient increments Δc that are used in the comprehensive code at the next iteration $n+1$ are calculated. The increments are the difference between the CFD loads and the comprehensive lifting line solution required to trim from the previous step n, plus the load increments from the previous step:

$$\Delta c^{n+1} = \Delta c^{n} + (c_{\text{CFD}} - c_{\text{total}}). \tag{3}$$

For the initial step, the increments are the difference between CFD and the total loads from the 0^{th} run in CAMRAD II:

$$\Delta c^{1} = c_{\text{CFD}} - c_{\text{total}}. \tag{4}$$

The sectional pitching moment $M^2 c_m$, normal force $M^2 c_n$, and chord force $M^2 c_c$ coefficients are defined as:

$$M^2 c_m = \frac{M'}{1/2 \rho a^2 c}, \tag{5}$$

$$M^2 c_n = \frac{N'}{1/2 \rho a^2 c}, \tag{6}$$

$$M^2 c_c = \frac{C'}{1/2 \rho a^2 c}. \tag{7}$$

With the new quarter chord motions of the retrimmed rotor and the new aircraft attitude, the CFD is rerun. The previous CFD flow solution is used as a restart condition. The coupling is performed every 1/3, 2/3 or full revolution. The coupling solution is considered to be converged when collective and cyclic control angles and the CFD aerodynamic forces do not change between iterations. The CFD flow solution is usually converged after 10 to 20 rotor revolutions. The coupling procedure is valid as long as the rotor loads are periodic. This approach is still good if there is some aperiodicity in the vortex wake, which is often the case in high-resolution turbulent simulations.

Aeroacoustic Analysis

The noise calculations are performed with the ANOPP2 (Ref. 15) and AeroAcoustic ROtor Noise (AARON) tools. AARON is a user code developed to perform rotorcraft noise calculation with ANOPP2. AARON/ANOPP2 can be used to calculate the loading noise, thickness noise and broadband noise using the information from a rotorcraft comprehensive code such as CAMRADII, or from a high-fidelity CFD solution from OVERFLOW.

The methodology used in this work follows the RVLT toolchain (Ref. 5). CAMRAD II calculates the azimuthal variations of the lifting-line loadings and motions, which are then used in the acoustic tools. A compact loading formulation (consistent with the lifting-line aerodynamic model) calculates the aerodynamically generated sound of the rotor via the blade sound sensors. Thickness noise is calculated using geometry information from the blade sound sensor and user inputs with a compact monopole model. An airfoil self-noise model extended to rotating blades is used for broadband noise.

Farassat's Formulation 1A (F1A) (Ref. 22) solution to the Ffowcs-Williams and Hawkings equation is used in ANOPP2. Farassat's solution is the most common approach used in rotorcraft noise analysis. One of the main assumptions for F1A is that the quadrupole term is neglected, leaving only the thickness and loading surface terms.

CAMRAD II FREE WAKE RESULTS

This section presents an initial study using the free wake analysis with the rotorcraft comprehensive code CAMRAD II for the QSMR. The free convecting wake can predict the performance more accurately than other models like uniform inflow. In addition, blade-vortex interaction (BVI) airloads are important to capture for noise calculations. First incorporated into the code in 1994 (Ref. 23), CAMRAD II free wake model has been validated extensively over the years.

The flight conditions are summarized in Table 3, which are representative of a UAM mission. Both low-noise without and with droop configurations are run using the same flight conditions.

Table 3: Flight conditions for the QSMR urban air taxi simulations.

Parameter	Baseline	Low-noise
h	5000 ft	5000 ft
T_∞	ISA 20°C	ISA 20°C
Ω	41.3 rad/s	25.5 rad/s
V_{tip}	213.36 m/s	137.16 m/s
M_{tip}	0.616	0.396
V_∞	99.52 kts	101.38 kts
M_∞	0.148	0.151
Re	1.6×10^6	1.3×10^6

Performance Analysis

Free wake CAMRAD II simulations for the QSMR are run on a single processor for the baseline, low-noise no droop, and low-noise 30° droop QSMR vehicles, in hover and cruise conditions.

The rotor wake tip vortices are plotted in Figure 6 for the hover simulations. The baseline geometry (Figure 6a) shows three tip vortices, with blade-vortex interactions (BVI). BVI happens when the vortex shed by the previous blade impinges on the current blade, creating unsteady pressure fluctuations mainly near the leading edge. As the number of blades increases, a more complex wake is formed (Figures 6b and 6c). Wake

instabilities are observed for the low-noise configurations. The wakes are plotted for three rotor revolutions.

The hover efficiency is measured in terms of the figure of merit (FM). The FM is the ratio between the ideal power to hover and the actual power required to hover. The calculated figures of merit for the different configurations are summarized in Table 4. Both the main rotor and aircraft FM are shown in this Table. The aircraft FM is slightly higher for the three cases. Very similar performance values are found in hover for the three geometries.

The effective lift-to-drag L/D_e ratio measures the cruise efficiency. The aircraft effective lift-to-drag ratio is defined as:

$$\frac{L}{D_e} = \frac{WV_\infty}{P}, \tag{8}$$

where W is the aircraft weight, V_∞ the freestream velocity and P is the power. The rotor L/D_e is:

$$\frac{L}{D_e} = \frac{LV_\infty}{P_0 + P_i}, \tag{9}$$

with L being the rotor lift, P_0 the profile power and P_i the induced power. The L/D_e for each configuration simulated are summarized in Table 5. The baseline configuration has the best cruise performance, with a rotor $L/D_e = 8.45$. Low-noise configurations perform worse, with a decrease in rotor performance of 21% between the baseline and low-noise 0° droop and of 45% between the baseline and low-noise 30° droop.

Table 4: Figure of merit obtained from free wake calculations with CAMRAD II.

Parameter	Baseline	Low-noise 0°	Low-noise 30°
FM aircraft	0.802	0.798	0.811
FM rotor	0.778	0.762	0.780

Table 5: Effective aircraft and rotor lift-to-drag ratios obtained from free wake calculations with CAMRAD II.

Parameter	Baseline	Low-noise 0°	Low-noise 30°
L/D_e aircraft	6.333	5.267	3.925
L/D_e rotor	8.453	6.644	4.638

Acoustic Analysis

Acoustics calculations have been performed using CAMRAD II free wake solution as data to run AARON/ANOPP2 following RVLT toolchain methodology. The calculations are performed with a single observer point located at located 150 m ahead and 150 m below the vehicle.

The acoustic pressures in hover and cruise for the three configurations are shown in Figures 7 and 8, respectively, for the time of one rotor revolution. The effect of reducing the tip speed on the acoustic pressure can be observed very clearly: the low-noise configurations have lower acoustic pressure amplitudes. Both in hover and in cruise, the thickness noise —due to fluid displacement by the surface, i.e., geometry dependent— is a smaller contribution than the loading noise —due to force exerted on the surrounding fluid by the surface, i.e., force dependent— to the total acoustic pressure. The baseline geometry shows strong BVI events, as seen in Figure 8a by the three peak-and-troughs. With a lower tip speed and six blades instead of three, the low-noise configuration without droop shows six weaker BVI events, Figure 8b. Adding 30° droop decreases BVI strength further (Figure 8c).

The metric to characterize acoustics in this work has been the Sound Pressure Level (SPL), defined as:

$$\mathrm{SPL} = 20\log_{10}\left(\frac{p_{\mathrm{rms}}}{p_0}\right)\,[\mathrm{dB}], \tag{10}$$

where p_{rms} is the pressure that has been frequency weighted and $p_0 = 20\,\mu\mathrm{dB}$ is the reference pressure.

The SPL for all configurations simulated with CAMRAD II, in hover and in cruise, are shown in Figure 9. The simulations in hover give quieter results that in cruise. The low-noise configuration is around 8 dB quieter than the baseline. The droop in hover does not change much the SPL. In cruise, an improvement of 8 dB is again observed between the baseline configuration and the low-noise configuration without droop. In this case, adding the 30° droop additionally improves the SPL by approximately 3 dB, with a total decrease of 11 dB when compared to the baseline geometry. This is a similar behaviour to that observed by Johnson (Ref. 6), where EPNL decreased by 12 dB.

COUPLED CAMRAD II–OVERFLOW RESULTS

In this section, a performance analysis of the high-fidelity CFD results run with OVERFLOW coupled with CAMRAD II will be presented, for the three QSMR vehicle configurations, in hover and in cruise, with the flight conditions depicted in Table 3.

The high-fidelity simulations have been carried out using NASA's supercomputers Pleiades, Electra, and Aitken. The number of cores ranges from 2000 to 2200, and simulations run from 8 to 15 days until convergence was obtained.

For the loose-coupling approach, CAMRAD II needs only to be run using uniform inflow, as the aerodynamics are replaced with the OVERFLOW airloads.

Hover Performance

Hover simulations are carried out with a simulated atmosphere at $h = 5000\,\mathrm{ft}$ and $T_\infty = \mathrm{ISA} + 20\,^\circ\mathrm{C}$. The loose-coupling approach is considered converged when the delta airloads have a relatively small change between coupling iterations. This reflects in the variation of the trim angles.

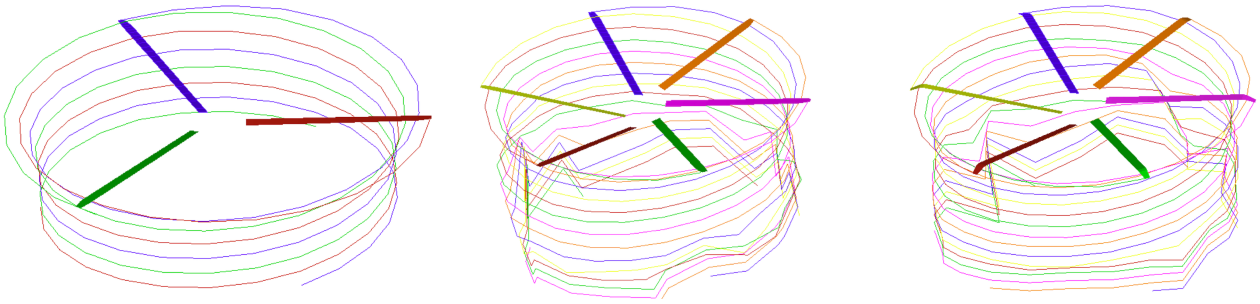

(a) Baseline geometry. (b) Low-noise geometry, no blade droop. (c) Low-noise geometry, 30° blade droop.

Figure 6: Wake geometry from CAMRAD II free wake solver. Figure 6a shows the baseline case; Figure 6b, the low-noise no blade droop case; and Figure 6c, the low-noise 30° blade droop case.

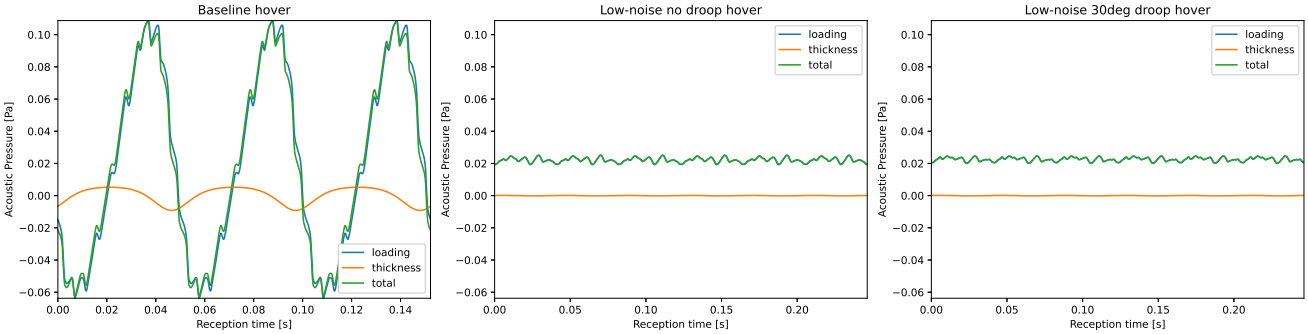

(a) Baseline geometry. (b) Low-noise geometry, no blade droop. (c) Low-noise geometry, 30° blade droop.

Figure 7: Thickness, loading, and total acoustic pressures in hover, at an observer located 150 m ahead and 150 m below the vehicle.

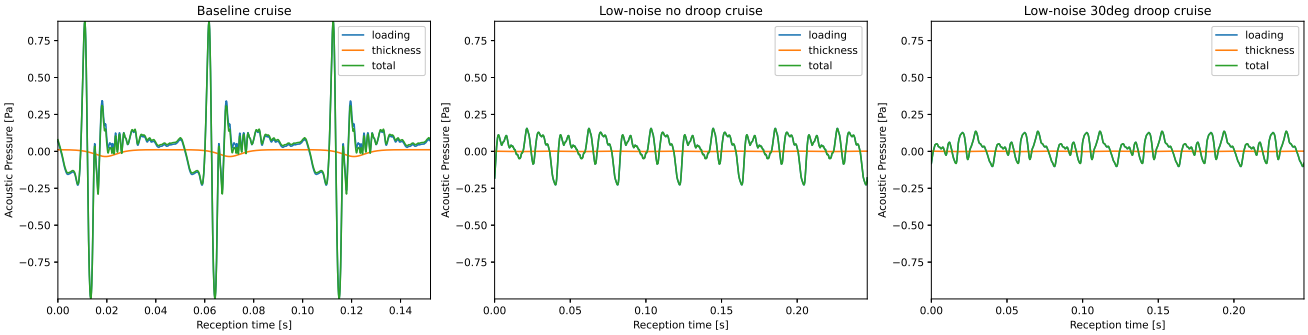

(a) Baseline geometry. (b) Low-noise geometry, no blade droop. (c) Low-noise geometry, 30° blade droop.

Figure 8: Thickness, loading, and total acoustic pressures in cruise, at an observer located 150 m ahead and 150 m below the vehicle.

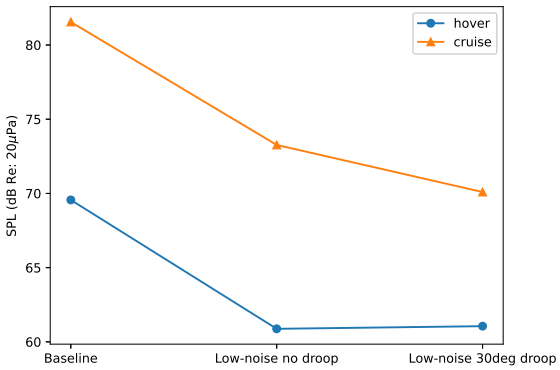

Figure 9: Sound Pressure Level (SPL), in hover and in cruise, for the three QSMR configurations. The low-noise 30° blade droop vehicle is 11 dB quieter.

The trim angles in hover are depicted in Figure 10 for the baseline (Figure 10a), low-noise no droop (Figure 10b), and low-noise 30° droop (Figure 10c). Good convergence is achieved after 5 to 10 coupling steps. The collective θ_0, coning angle β_0, lateral flapping β_{1s}, and longitudinal flapping β_{1c} angles are shown in this image. Higher collective and coning angles are obtained for the low-noise configurations compared to the baseline geometry.

The normal force coefficient, chord force coefficient, and pitching moment coefficient on the rotor disk are plotted in Figure 11. And almost axisymmetric flow can be observed on the airloads distributions, with some aerodynamic interactions near the ψ =0° region from the vehicle's tail, more clearly seen in the baseline geometry. Rotor-tail interactions are more clearly observed in Figures 11a and 11d. The baseline configuration shows relatively higher values of normal and chord force coefficients than the low-noise QSMR vehicle configurations. The droop decreases the force coefficient values near the tip. Pitching moment coefficient is small throughout the disk.

Q-criterion vorticity iso-surfaces colored with the vorticity magnitude are shown in Figure 12 for the three geometries. The wake geometry in hover can be observed in the images. Vortex wake breakdown happens after 2 to 4 revolutions. There is a similar vorticity magnitude on the vortices between the baseline and low-noise no-droop configurations (Figures 12a 12b). The tip droop changes the position of the primary tip vortex and decreases its strength, as seen by the lower vorticity magnitude (Figure 12c). In addition, a secondary weak vortex is formed where the droop starts, due to the change in aerodynamic distribution at that section of the blade. A closer view of these phenomena is presented in Figure 13. In the images, it can be observed in detail BVI in hover for the three cases, with the drooped rotor having the secondary vortices (Figure 13c). In Figure 14, the vorticity magnitude contours at a plane located at $y = 0$ are shown. In the images, the rotor-airframe interactions can be clearly observed near the tail region. The wake contraction is affected by the tail and reflected on the right side of the images, where the symmetry of the wake is broken. Flow separation from the airframe can also be observed.

The aircraft and rotor figure of merit have been calculated for the coupled CAMRAD II-OVERFLOW simulations in hover. The results are gathered in Table 6. Very similar values to the free wake results from Table 4 obtained from CAMRAD II free wake solver. In particular, the FM for the baseline geometry using OVERFLOW-CAMRAD II is around 5% lower compared to the free wake results. For the low-noise geometries, higher FM values are obtained when using OVERFLOW, of between 3% to 5% difference. From these results, the low-noise geometry without droop is slightly the most efficient configuration in hover.

Table 6: Figure of merit obtained from high-fidelity CFD simulations using OVERFLOW coupled with CAMRAD II for trim and rotor blade motions.

Parameter	Baseline	Low-noise 0°	Low-noise 30°
FM aircraft	0.769	0.828	0.812
FM rotor	0.736	0.803	0.782

Cruise Performance

The cruise simulations are performed at the same altitude and temperature as the hover case, with $V_\infty = 99.52$ kts (advance ratio $\mu = {}^{V_\infty}/_{\Omega R} = 0.24$) for the baseline geometry and $V_\infty = 101.38$ kts ($\mu = 0.38$) for the low-noise vehicles.

The trim angles solution is shown in Figure 15. The baseline geometry loose-coupling converges fast, and there is not much variation with the initial trim solution from CAMRAD II, see Figure 15a. Lateral and longitudinal flapping are small and similar in the baseline geometry. The low-noise configurations (Figures 15b and 15c) take 10-15 coupling steps to converge, yielding higher collective angles θ_0, with a high value of $\theta_0 = 15.7°$ for the low-noise configuration with 30° droop.

The airloads on the rotor disk in cruise are depicted in Figure 16. The first row of images shows the normal force coefficient $M^2 c_n$ (Figures 16a, 16b, and 16c), the middle row shows the chord force coefficient $M^2 c_c$ (Figures 16d, 16e, and 16f), and the last row shows the pitching moment coefficient $M^2 c_m$ (Figures 16g, 16h, and 16i). In cruise, the airloads are no longer axisymmetric. Comparing the baseline and low-noise without droop configurations (first and second columns of Figure 16), higher normal and chord force coefficients are obtained for the baseline geometry. Between the low-noise without droop and the 30° droop vehicles, the configuration with droop results in higher force coefficients as well, due to the higher trim solution for θ_0. For the three-bladed rotor, a strong BVI is observed near $\psi = 270°$. Another BVI event can be observed around $\psi = 90°$. For the low-noise configurations, the two BVI events are not so clear in the airloads distributions. A BVI event around $\psi = 180°$ is observed in both cases, stronger for the blade with droop.

Figure 17 depicts the vortex wake for the three QSMR configurations in cruise by plotting the Q-criterion vorticity iso-surfaces colored with the vorticity magnitude. BVI events

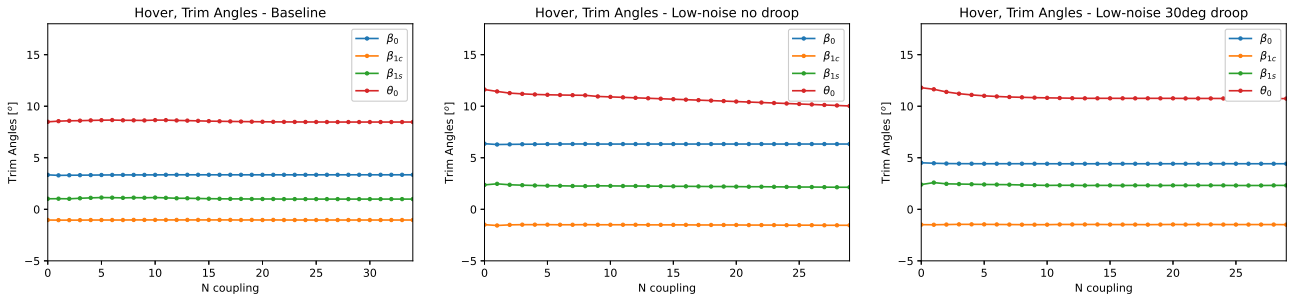

(a) Baseline geometry. (b) Low-noise, 0° blade droop geometry. (c) Low-noise, 30° blade droop geometry.

Figure 10: Trim angles as a function of the coupling step in hover.

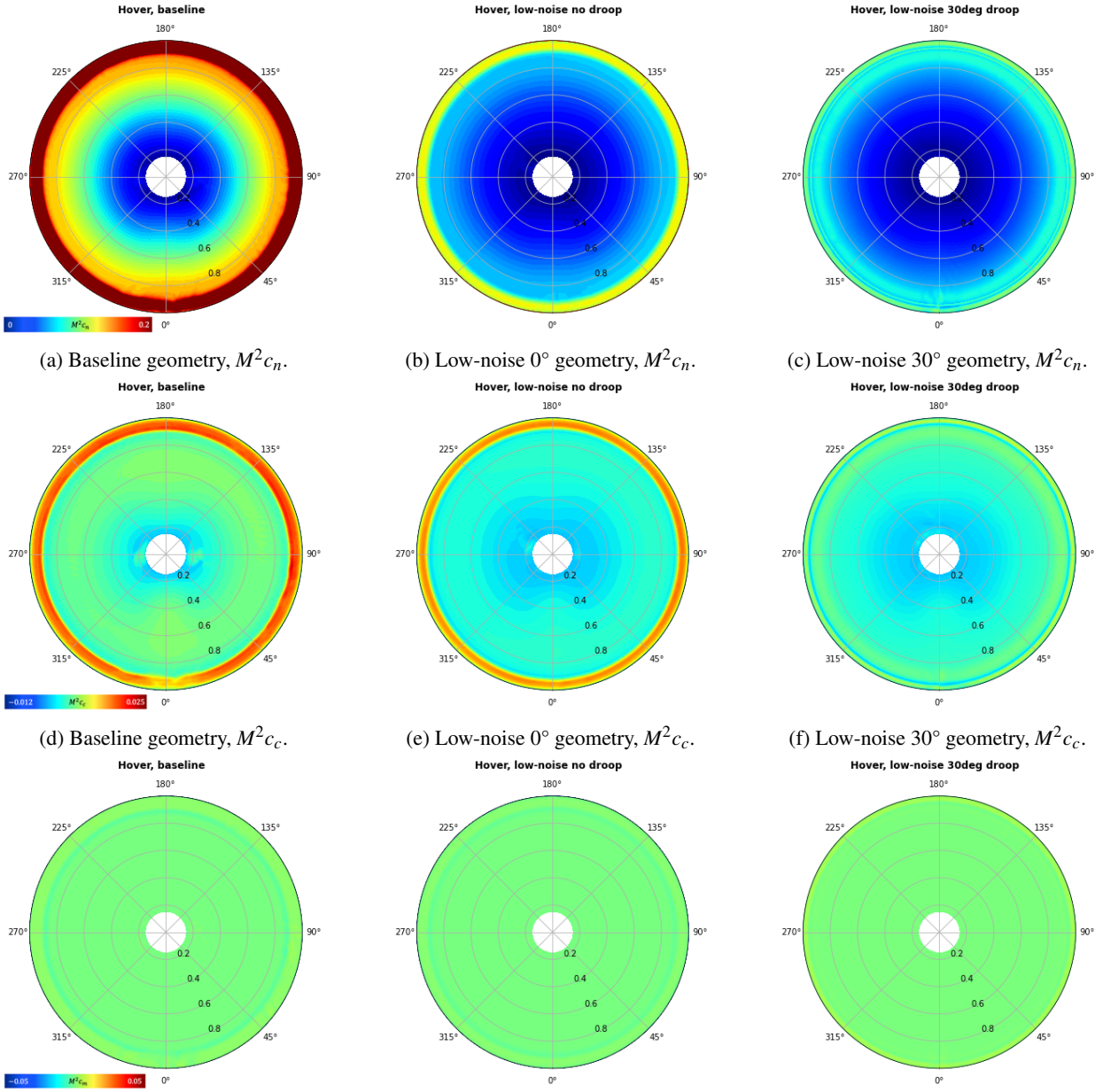

(a) Baseline geometry, M^2c_n. (b) Low-noise 0° geometry, M^2c_n. (c) Low-noise 30° geometry, M^2c_n.

(d) Baseline geometry, M^2c_c. (e) Low-noise 0° geometry, M^2c_c. (f) Low-noise 30° geometry, M^2c_c.

(g) Baseline geometry, M^2c_m. (h) Low-noise 0° geometry, M^2c_m. (i) Low-noise 30° geometry, M^2c_m.

Figure 11: Rotor disk airloads in hover.

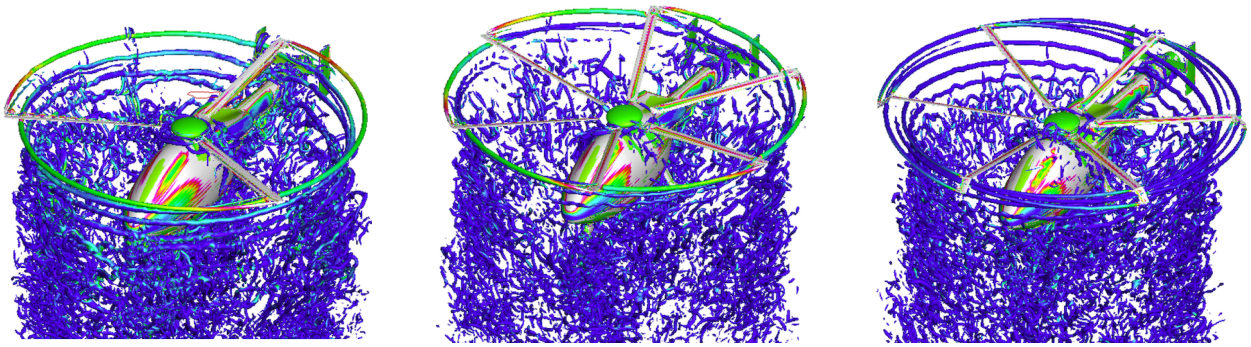

(a) Baseline geometry. (b) Low-noise geometry no blade droop. (c) Low-noise geometry 30° blade droop.

Figure 12: QSMR wake geometry obtained from OVERFLOW in hover. Q-criterion vorticity iso-surfaces colored with the vorticity magnitude, oblique view. Figure 12a shows the baseline case. Figure 12b shows the low-noise no blade droop case. Figure 12c shows the low-noise 30° blade droop case.

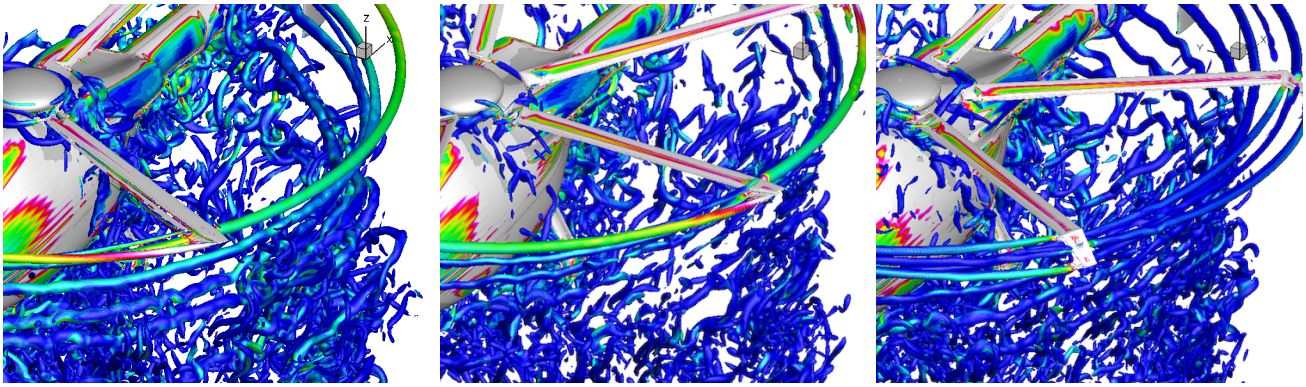

(a) Baseline geometry. (b) Low-noise geometry no blade droop. (c) Low-noise geometry 30° blade droop.

Figure 13: QSMR wake geometry obtained from OVERFLOW in hover. Q-criterion vorticity iso-surfaces colored with the vorticity magnitude. Close-up view to show the blade tip vortices. Figure 13a shows the baseline case. Figure 13b shows the low-noise no blade droop case. Figure 13c shows the low-noise 30° blade droop case.

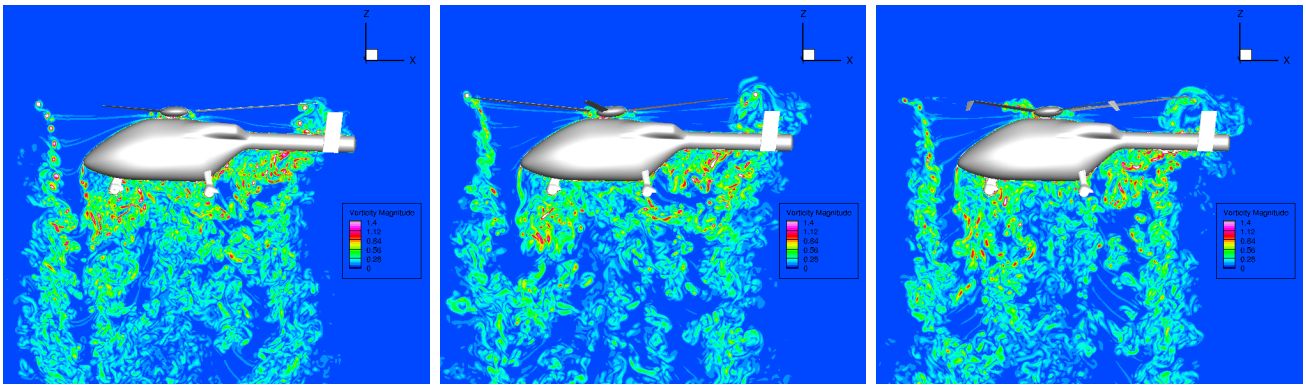

(a) Baseline geometry. (b) Low-noise geometry, no blade droop. (c) Low-noise geometry, 30° blade droop.

Figure 14: Vorticity magnitude contours at a plane located at $y = 0$ for the QSMR vehicle in hover.

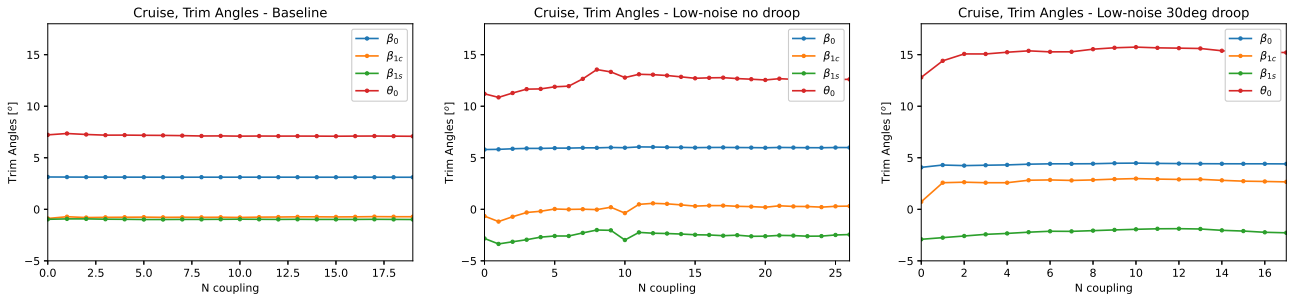

(a) Baseline geometry. (b) Low-noise, 0° blade droop geometry. (c) Low-noise, 30° droop geometry.

Figure 15: Trim angles as a function of the coupling step in cruise.

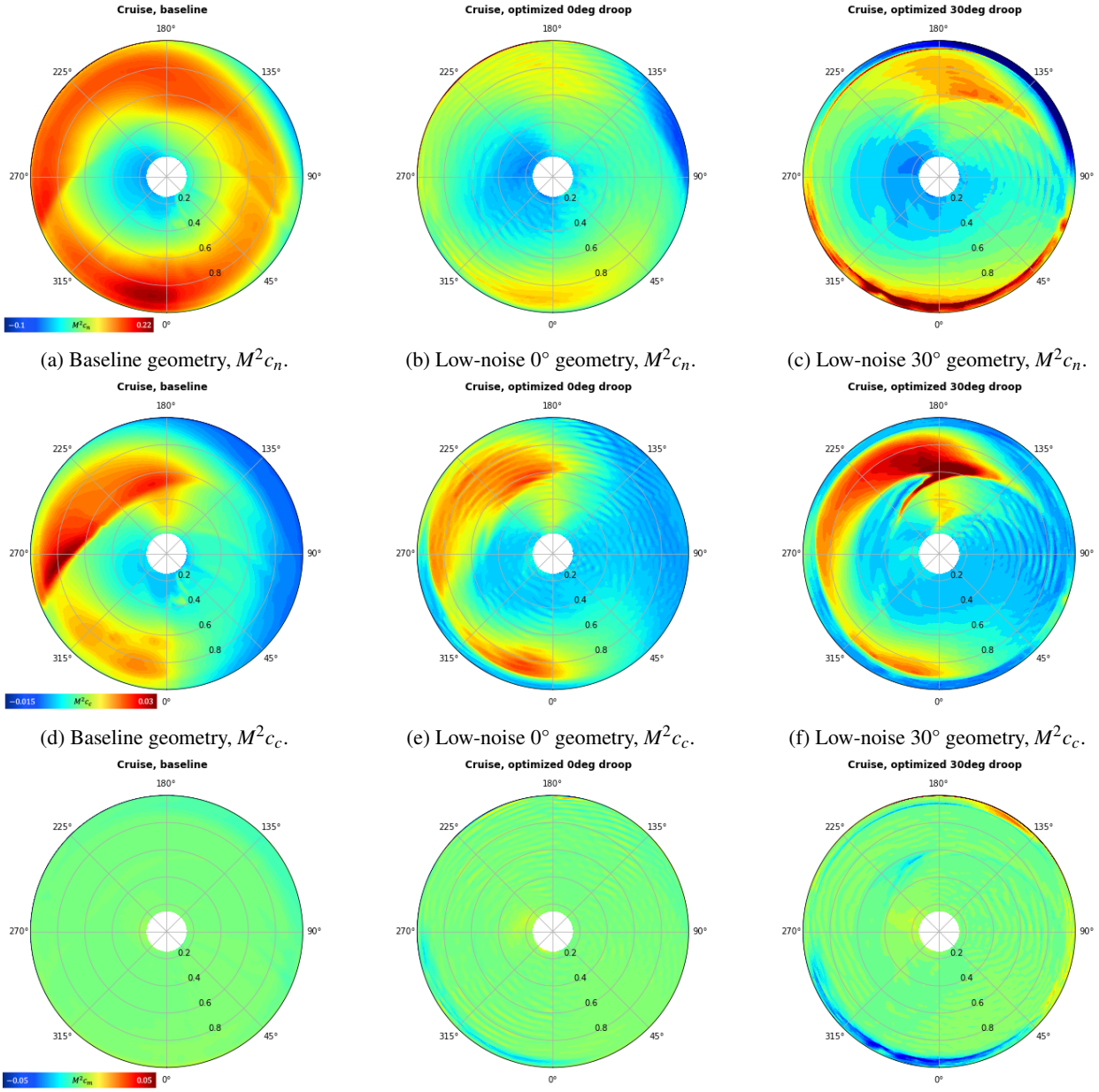

(a) Baseline geometry, M^2c_n. (b) Low-noise 0° geometry, M^2c_n. (c) Low-noise 30° geometry, M^2c_n.

(d) Baseline geometry, M^2c_c. (e) Low-noise 0° geometry, M^2c_c. (f) Low-noise 30° geometry, M^2c_c.

(g) Baseline geometry, M^2c_m. (h) Low-noise 0° geometry, M^2c_m. (i) Low-noise 30° geometry, M^2c_m.

Figure 16: Rotor disk airloads in cruise.

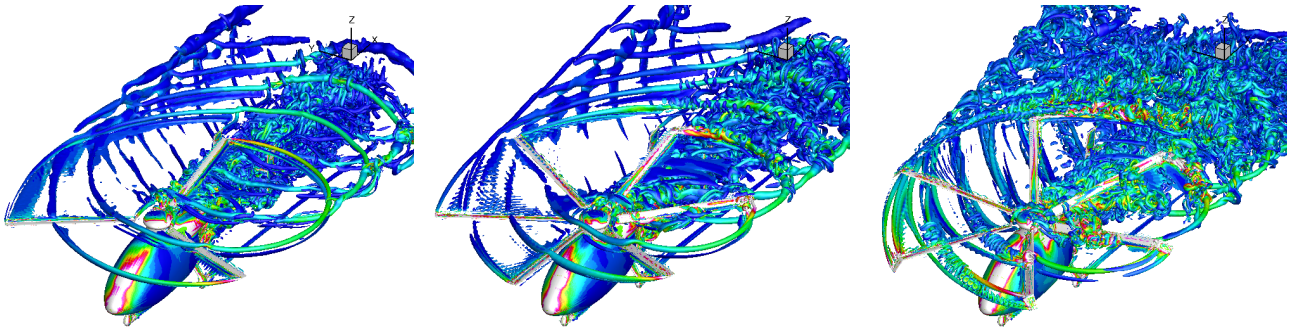

(a) Baseline geometry. (b) Low-noise geometry, no blade droop. (c) Low-noise geometry, 30° blade droop.

Figure 17: QSMR wake geometry obtained from OVERFLOW in cruise. Q-criterion vorticity iso-surfaces colored with the vorticity magnitude, oblique view. Figure 17a shows the baseline case. Figure 17b shows the low-noise no blade droop case. Figure 17c shows the low-noise 30° blade droop case.

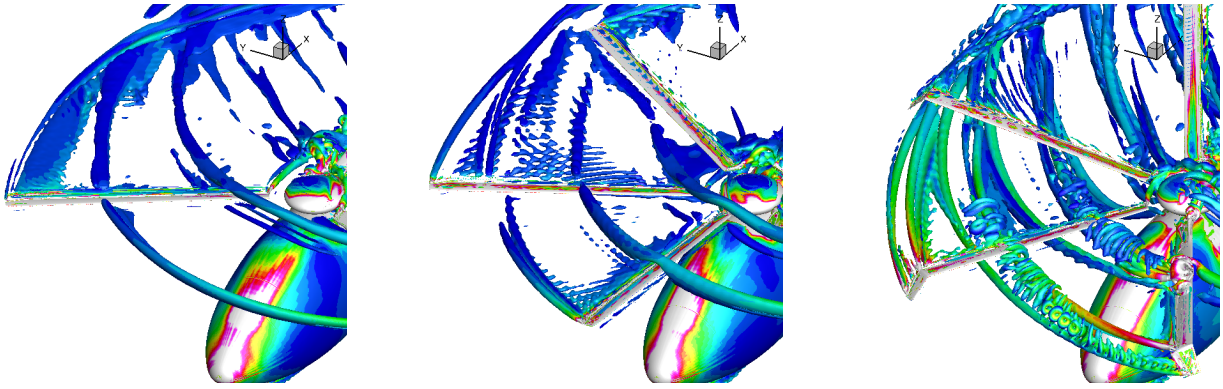

(a) Baseline geometry. (b) Low-noise geometry, no blade droop. (c) Low-noise geometry, 30° blade droop.

Figure 18: QSMR wake geometry obtained from OVERFLOW in cruise. Q-criterion vorticity iso-surfaces colored with the vorticity magnitude. Close-up view to show the blade tip vortices. Figure 18a shows the baseline case. Figure 18b shows the low-noise no blade droop case. Figure 18c shows the low-noise 30° blade droop case.

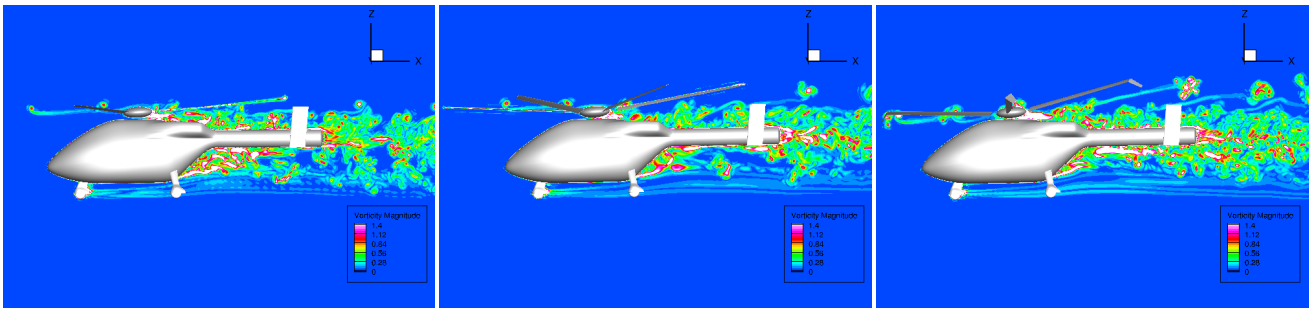

(a) Baseline geometry. (b) Low-noise geometry, no blade droop. (c) Low-noise geometry, 30° blade droop.

Figure 19: Vorticity magnitude contours at a plane located at $y = 0$ in cruise.

can be clearly observed in these images. The blade located at $\psi = 240°$ is near where the strong BVI event happens. This is a parallel BVI event, where the axis of the vortex is parallel to that of the blade. This type of BVI generates a strong impulsive noise, as it was observed in Figure 8a. Another BVI occurs around the second quadrant. This is a perpendicular BVI event, with the axis of the vortex perpendicular to the blade's axis and on the same plane. For the low-noise configurations (Figures 17b and 17c), another perpendicular BVI event can be observed near $\psi = 180°$. A more complex and turbulent wake is observed for the low-noise configuration with droop, due to the presence of the secondary vortices shed from the blade section where the droop begins. A closer view of the BVI events in the second quadrant and near $\psi = 180°$ is presented in Figure 18. The baseline configuration shows two perpendicular BVIs, from the vortices shed from the previous blades. The interactions near the blade root are weaker as it is an "older" vortex. A vortex sheet can also be observed. The low-noise vehicles with six blades show that there are twice the number of vortices. The wake appears to be more turbulent as well, with secondary vortices developing for the drooped blade. Higher vorticity is also observed on the iso-surfaces, probably due to the higher local angles of attack seen for the 30° droop blade vehicle. The vorticity magnitude contours are shown in Figure 19. The vortex cores and flow separation from the airframe and landing gear can be observed.

The effective aircraft and rotor lift-to-drag ratios are presented in Table 7. The same trend as observed with the free wake solver from CAMRAD II is obtained here. The baseline geometry has the highest effective lift-to-drag ratio, both for the aircraft and the rotor. Approximately, there is a 5% difference for the baseline geometry between the CAMRAD II free wake results and OVERFLOW results. However, the difference increases for the low-noise configuration, with a rotor L/D_e up to 30% lower for the low-noise 30° droop QSMR vehicle. This behavior on the L/D_e has been previously observed in (Ref. 8). Overall, the low-noise vehicles are less efficient in terms of L/D_e, with the low-noise drooped vehicle having 60% lower rotor lift-to-drag ratio than the baseline geometry.

Table 7: Effective aircraft and rotor lift-to-drag ratios obtained from high-fidelity CFD simulations using OVERFLOW coupled with CAMRAD II for trim and rotor blade motions.

Parameter	**Baseline**	**Low-noise 0°**	**Low-noise 30°**
L/D_e aircraft	5.997	4.263	2.790
L/D_e rotor	7.855	5.110	3.128

SUMMARY AND FUTURE WORK

NASA's RVLT QSMR vehicle has been simulated using comprehensive analysis, CAA, and high-fidelity CFD. Three vehicle configurations have been analyzed: the baseline, with a tip speed of V_{tip} =700 ft/s and three blades; the low-noise without droop, with V_{tip} =450 ft/s and six blades; and the low-noise with 30° droop.

Initially, CAMRAD II free wake solver has been run in hover and in cruise for the three configurations, finding that the figure of merit is very similar for the three cases. The effective aircraft and rotor lift-to-drag ratios revealed that the low-noise configurations perform worse in cruise than the baseline QSMR vehicle.

An acoustic analysis using AARON/ANOPP2 with CAMRAD II free wake results has been carried out. The acoustic pressures and the SPL have been obtained, showing a decrease of 11 dB of the low-noise with 30° droop compared to the baseline configuration. The acoustic pressures also showed BVI were relatively weaker for the low-noise configurations.

Then, loosely-coupled CAMRAD II-OVERFLOW simulations using NASA's supercomputers have been performed. The simulations were carried out on overset grids with more than half a billion grid points, used 2000 to 2200 processors, and run for several days until convergence was achieved. The airloads, final trim angles, wake geometries, and performance have been obtained. Lower tip speed on the low-noise vehicles produced weaker vortices. Similar performance was obtained in hover for the three configurations. The blade droop showed the formation of secondary wake tip vortices. Rotor-fuselage interactions were observed, mostly near the tail of the vehicle. In cruise, the baseline geometry was the most efficient in terms of the lift-to-drag ratio, following the same trend obtained with the free wake solver. Blade-vortex interactions were analyzed for the three geometries of this work.

A quieter vehicle can be obtained by changing the blade design and having lower tip speeds, without reducing the hover performance or increasing the vehicle's weight significantly. However, the cruise performance is affected by these design parameters, and an important decrease in the effective lift-to-drag ratio has been observed.

Some future work includes: the acoustic analysis using the surface data from high-fidelity CFD, the effect of vibrations on noise, and eventually replacing the loose-coupling methodology with CFD time-accurate computations.

ACKNOWLEDGMENTS

This work is supported by the Revolutionary Vertical Lift Technology (RVLT) Project (PM: Susan Gorton; TL: Brian Allan). The computations utilized the Pleiades, Electra, and Aitken supercomputers at the NASA Advanced Supercomputing Division. The authors would like to thank Wayne Johnson, Chris Silva, and Brian Allan, for helpful discussions.

REFERENCES

1. Yamauchi, G., "A Summary of NASA Rotary Wing Research: Circa 2008-2018", NASA/TP 2019-220459, December 2019.

2. Johnson, W. and Silva, C., "NASA concept vehicles and the engineering of advanced air mobility aircraft", The Aeronautical Journal 2022, 126, pp. 59-91. https://doi.org/10.1017/aer.2021.92

3. Johnson, W., Silva, C., and Solis, E., "Concept Vehicles for VTOL Air Taxi Operations", The AHS International Technical Meeting on Aeromechanics Design for the Transformative Flight, San Francisco, California, January 2018.

4. Johnson, W. and Silva, C.,"Observations from Exploration of VTOL Urban Air Mobility Designs", The Asian/Australian Rotorcraft Forum, Jeju Island, Korea, October 30 – November 1, 2018.

5. Silva, C. and Johnson, W., "Practical Conceptual Design of Quieter Urban VTOL Aircraft", VFS 77th Annual Forum, Virtual Event, May 2021.

6. Johnson, W., "A Quiet Helicopter for Air Taxi Operations", VFS Aeromechanics for Advanced Vertical Flight Technical Meeting, San Jose, CA, January 21–23, 2020.

7. Ventura Diaz, P., and Yoon, S., "Computational Study of NASA's Quadrotor Air Taxi Concept", AIAA Paper 2020-0302, The AIAA SciTech Forum 2020, Orlando, Florida, January 2020. https://doi.org/10.2514/6.2020-0302

8. Ventura Diaz, P., and Yoon, S., "High-Fidelity Simulations of a Quadrotor Vehicle for Urban Air Mobility", AIAA Paper 2022-0152, The AIAA SciTech Forum 2022, January 2022. https://doi.org/10.2514/6.2022-0152

9. Ventura Diaz, P., Johnson, W., Ahmad, J., and Yoon, S., "Computational Study of the Side-by-side Urban Air Taxi Concept", VFS 75th Annual Forum, Philadelphia, Pennsylvania, May 2019.

10. Ventura Diaz, P. and Yoon, S., "High-Fidelity Computational Aerodynamics of Multi-Rotor Unmanned Aerial Vehicles", AIAA Paper 2018-1266, The AIAA SciTech Forum 2018, Kissimmee, Florida, January 2018. https://doi.org/10.2514/6.2018-1266

11. Li, S. K. and Lee, S., "Acoustic Analysis of a Quiet Helicopter for Air Taxi Operations", VFS 77th Annual Forum, Virtual Event, May 2021.

12. Pulliam, T. H., "High Order Accurate Finite-Difference Methods: as seen in OVERFLOW", AIAA Paper 2011-3851, 20th AIAA Computational Fluid Dynamics Conference, Honolulu, Hawaii , June 2011. https://doi.org/10.2514/6.2011-3851

13. Chan, W. M., Gomez, R. J., Rogers, S. E., Buning, P. G., "Best Practices in Overset Grid Generation", AIAA Paper 2002-3191, The 32nd AIAA Fluid Dynamics Conference, St. Louis, Missouri, June 2002. https://doi.org/10.2514/6.2002-3191

14. Johnson, W., "Rotorcraft Aerodynamic Models for a Comprehensive Analysis", American Helicopter Society 54th Annual Forum, Washington, D. C., May 1998.

15. Lopes, L.V., and Burley, C.L., "ANOPP2 User's Manual: Version 1.2", NASA TM-2016-219342, 2016.

16. Haimes, R., and Dannenhoffer, J. F., "The Engineering Sketch Pad: A Solid-Modeling, Feature-Based, Web-Enabled System for Building Parametric Geometry", AIAA Paper 2013-3073, The 21st AIAA Computational Fluid Dynamics Conference, San Diego, California, June 2013. https://doi.org/10.2514/6.2013-3073

17. Yoon, S., Chaderjian, N. M., Pulliam, T. H., and Holst, T. L., "Effect of Turbulence Modeling on Hovering Rotor Flows", AIAA Paper 2015-2766, The 45th AIAA Fluid Dynamics Conference, Dallas, Texas, June 2015. https://doi.org/10.2514/6.2015-2766

18. Yoon, S., Lee, H. C., and Pulliam, T. H., "Computational Analysis of Multi-Rotor Flows", AIAA Paper 2016-0812, The 54th AIAA Aerospace Sciences Meeting, AIAA SciTech Forum, San Diego, California, January 2016. https://doi.org/10.2514/6.2016-0812

19. Yoon, S. Lee, H. C., and Pulliam, T. H., "Computational Study of Flow Interactions in Coaxial Rotors", The AHS Technical Meeting on Aeromechanics Design for Vertical Lift, San Francisco, California, January 2016.

20. Spalart, P. R., Jou, W-H., Strelets, M., and Allmaras, S. R., "Comments on the Feasibility of LES for Wings and on a Hybrid RANS/LES Approach", Advances in DNS/LES, Greyden Press, 1997, pp. 137-147.

21. Spalart, P. R., "Strategies for Turbulence Modeling and Simulations", International Journal of Heat and Fluid Flow, 21, 2000, pp. 252-263.

22. Farassat, F., "Linear Acoustic Formulas for Calculation of Rotating Blade Noise", AIAA Journal, Vol. 19, No. 9, September 1981, pp. 1122–1130

23. Johnson, W., "Technology Drivers in the Development of CAMRAD II", American Helicopter Society Aeromechanics Specialist Meeting, January 1994.